Switched Active Power Control of a Grid-Connected Inverter With Reduced RoCoF and Frequency Overshoot

Yuan Chen, Bo Zhang, *Fellow, IEEE*, Dongyuan Qiu, *Senior Member, IEEE*, Yanfeng Chen, *Member, IEEE*, Fan Xie, *Member, IEEE*, and Huadong Sun, *Senior Member, IEEE*

***Abstract*—In this article, a switched active power control of the grid-connected inverter is proposed. First, the principle of the proposed control is demonstrated with the phase trajectory analysis. The proposed control allows for direct adjustment of the maximum rate of change of frequency (RoCoF) and frequency overshoot of the inverter, thereby enhancing the frequency stability. Next, the stability of the proposed control is examined using the Lyapunov function. For the active power control loop of the inverter, the proposed control has been proven to ensure global asymptotic stability. Then, the parameters of the proposed control are designed. Due to the clear physical meaning, the proposed control allows for explicit derivation of the relationships among RoCoF, frequency overshoot, response time, and active power overshoot of the inverter. Therefore, the controller parameters can be directly designed using the derived analytical equations, simplifying the application of the proposed control. Finally, the proposed control is clarified through detailed comparisons to highlight its advantages. The proposed control achieves a lower RoCoF and frequency overshoot compared to existing controls while maintaining the same active power overshoot and response time. This is demonstrated through theoretical, simulation, and experimental results.**

***Index Terms*—Frequency stability, grid-connected inverter, rate of change of frequency (RoCoF), switched control, virtual synchronous generator (VSG).**

I. Introduction

DISTRIBUTION generators are widely used in power system applications, such as solar photovoltaic [1], [2] and wind-driven generators [3], [4], [5]. The output voltages of these generators, unlike those of synchronous generators, are either dc or unregulated ac. Therefore, the grid-connected inverters, namely the grid-following inverter and the grid-forming inverter, are typically connected between the distribution generator and the power grid [6], [7]. Among them, the grid-forming inverter has garnered significant attention from a diverse range of researchers owing to its grid-forming ability [8], [9], [10].

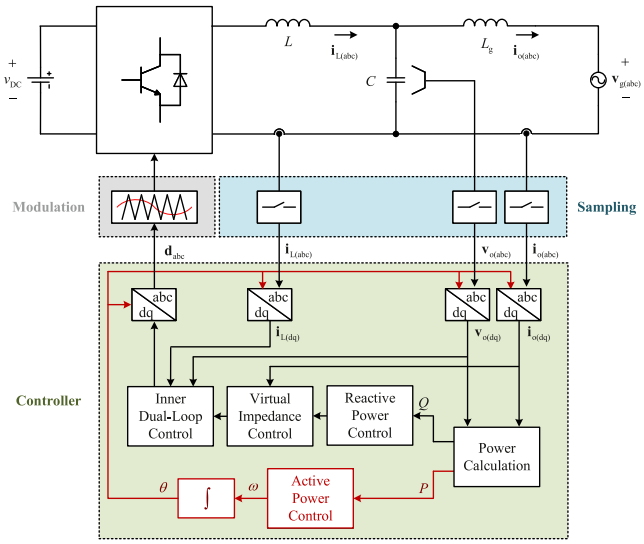

Fig. 1. General structure of a grid-forming inverter.

The general structure of a grid-forming inverter, as shown in Fig. 1, consists mainly of the inner dual-loop control, optional virtual impedance control, reactive power control, and active power control. The aforementioned four parts have seen the publication of many good and interesting works, which are currently hot topics. However, for an article, if the concern is so broad, it is nearly impossible to make progress on any specific topic. Therefore, this article focuses on the active power control labeled in red in Fig. 1.

Traditionally, the active power control of the grid-forming inverter is achieved through the droop control [11], [12], [13], where the local frequency reference is decided by proportional feedback. Compared to the traditional synchronous generator, the grid-connected inverter with droop control has a higher rate of change of frequency (RoCoF) and frequency overshoot. The characteristics of the power grid are determined by the connected power source. Therefore, the increasing proportion of grid-connected inverters in the power grid leads to higher RoCoF and frequency overshoot, resulting in a lower frequency

Manuscript received 27 September 2023; revised 11 December 2023; accepted 25 December 2023. Date of publication 4 January 2024; date of current version 16 February 2024. This work was supported by the National Natural Science Foundation of China under Grant U2166601. Recommended for publication by Associate Editor S. Golestan. *(Corresponding author: Bo Zhang.)*

Yuan Chen, Bo Zhang, Dongyuan Qiu, Yanfeng Chen, and Fan Xie are with the School of Electric Power, South China University of Technology, Guangzhou 510640, China (e-mail: yuanchensd@163.com; epbzhang@scut.edu.cn; epdyqiu@scut.edu.cn; eeyfchen@scut.edu.cn; epfxie@scut.edu.cn).

Huadong Sun is with the State Key Laboratory of Power Grid Safety and Energy Conservation, China Electric Power Research Institute, Beijing 100192, China (e-mail: sunhd@epri.sgcc.com.cn).

Color versions of one or more figures in this article are available at https://doi.org/10.1109/TPEL.2024.3349632.

Digital Object Identifier 10.1109/TPEL.2024.3349632

nadir [14], [15], [16]. These frequency characteristics can lead to the operation of RoCoF relay protection and the instability of the power grid [17], [18], [19].

The aforementioned problems can be avoided through two main methods. One method is maintaining a high proportion of synchronous machines in the power grid. Their rotor and damping winding can limit their RoCoF and frequency overshoot naturally and enhance the frequency stability of the power grid. Another method is controlling the grid-connected inverter to reshape its frequency characteristics. The control method should limit the RoCoF and frequency overshoot of the grid-connected inverter to reduce their negative impact on power grid stability. This article focuses on the second method, with virtual synchronous generator (VSG) control as a typical representative [20], [21], [22], [23].

In the VSG, the active power control loop is designed similarly to a real synchronous generator, aiming to reduce RoCoF and frequency overshoot. However, recent research [24], [25], [26], [27], [28], [29], [30], [31] indicates that inverters with VSG control experience significant active power overshoot and response time, which limits their application. On the one hand, the large active power overshoot causes the current saturation (CS) problem [24], leading to transient instability and weakening the VSG's ability to enhance the frequency stability. To avoid this problem, the current limit of the inverter needs to be increased. Correspondingly, the selection of inverter devices with VSG control must be made with a significant margin, thereby increasing both size and cost. On the other hand, the large response time hampers the primary and secondary frequency modulation ability of the inverter.

Nowadays, the performance of the VSG control has been continuously improved through high-order linear control [25], self-adaptive VSG control [26], [27], [28], [29], fractional-order VSG control [30], and H_∞ control [31]. The high-order linear control [25] and fractional-order VSG control [30] allow for adjusting additional coefficients, such as the controller's order, to enhance flexibility in design and achieve superior performance. The self-adaptive VSG control [26], [27], [28], [29] achieves diverse design requirements by using different inertia and damping coefficients in various states. The H_∞ control [31] enables obtaining optimized controller parameters based on the H_∞ theory to enhance the inverter performance. These controls can achieve better frequency stability than the original VSG control, with lower RoCoF and frequency overshoot.

However, the aforementioned controls are not sufficient to fully solve the problems in VSG controls. On the one hand, the aforementioned controls primarily rely on transfer functions in the s-domain or the z-domain. For the stability analysis, these transfer functions are readily comprehensible. However, the objective of enhancing VSG control is to achieve a control system with reduced RoCoF and frequency overshoot, both of which are control targets in the time domain. Based on the state-space model in the time domain, the control method with lower RoCoF and frequency overshoot can be obtained, which is lacking in existing research. On the other hand, existing controls based on transfer functions typically employ complex exponential or transcendental functions to express the relationships among control parameters, active power overshoot, response time, RoCoF, and frequency overshoot, resulting in a complicated parameter design process. The application needs a control method and controller design process that are simpler and have clearer physical meaning.

To solve the aforementioned problems in existing research, this article introduces the switch control theory into the active power control design of the grid-connected inverter and proposes a switched active power control with reduced RoCoF and frequency overshoot. The main contribution can be summed as follows.

1) A standard state-space model is proposed to represent the active power characteristics of the grid-forming inverter. Based on this model and the phase trajectory analysis, a switched active power control is designed, allowing direct adjustment of maximum RoCoF and frequency overshoot to enhance frequency stability.
2) Based on the Lyapunov function, a stability analysis of the proposed control is made. For the active power control loop, the Lyapunov function of the inverter with the proposed control decreases monotonously in the whole phase plane, resulting in global asymptotic stability.
3) The relationship among the RoCoF, frequency overshoot, response time, and active power overshoot of the inverter with the proposed control is derived explicitly. The proposed control has a clear physical meaning, allowing for the direct design of controller parameters using derived analytical equations. This simplifies the application of the control.
4) The inverters employing the proposed control are compared in detail to those employing existing controls. The proposed control achieves a lower RoCoF and frequency overshoot compared to existing controls while maintaining the same active power overshoot and response time. This is demonstrated through theoretical, simulation, and experimental results.

The rest of this article is organized as follows. The principle of the proposed switched active power control is derived in Section II. The controller parameters are designed in Section III. The proposed control is compared with existing similar controls in Section IV. All the aforementioned analyses and comparisons are verified by the simulation and experiment results in Section V. Finally, Section VI concludes this article.

II. Switched Active Power Control

In this section, a standard state-space model is first derived to represent the frequency characteristic of the inverter connected with the power grid. Then, the phase trajectories of the inverter with different RoCoF inputs are analyzed. Finally, a switched active power control is proposed by the phase trajectory analysis and its stability is analyzed by the Lyapunov function. To simplify analyses, several assumptions are made as follows, which are also used in previous works [25], [26], [27], [28], [29], [30], [31].

1) The response speed of the voltage and current inner control loop is much faster than that of the active power control

loop, rendering their coupling negligible. As shown in Fig. 1, the controller in the grid-forming inverter consists of multiple parts and is a high-order system. With this assumption, the active power control loop of the grid-connected inverter can be analyzed individually as a two-order system.

2) The resistance of the power transmission line is much lower than its inductive reactance, and the power grid can be seen as inductive. With this assumption, the active and reactive power loop is decoupled.
3) The analyzed distribution generators participate in the primary frequency control and have sufficient energy reserves to meet the power requirement.
4) As the active power reference and grid frequency remain constant values at a steady state, the analysis and controller design are mainly made for their step changes. Therefore, the situation with periodic changes in grid frequency and active power reference is not discussed here.

A. Standard State-Space Model

For the inverter connected to the power grid, to achieve synchronization and primary frequency control, the steady values of the active power and angular frequency are

$$\begin{cases} P(t_{\mathrm{S}}) = P_{\mathrm{S}} = P_0 - k_{\mathrm{p}}(\omega_{\mathrm{g}} - \omega_0) \\ \omega(t_{\mathrm{S}}) = \omega_{\mathrm{S}} = \omega_{\mathrm{g}} \end{cases} \tag{1}$$

where P_{S} is the steady value of the active power, ω_{S} is the steady value of the angular frequency, t_{S} is the steady time point, ω_0 is the nominal value of the angular frequency, ω_{g} is the grid angular frequency, P_0 is the nominal value of the active power, and k_{p} is the droop coefficient of the primary frequency control.

In this article, the state variables in the state-space model are defined as the deviations between their actual values and their steady-state values. Therefore, the final values of all state variables are 0, facilitating a uniform description and discussion. With the aforementioned consideration, the state variables are

$$\mathbf{x} = \begin{bmatrix} \Delta P & \Delta\omega \end{bmatrix}^{\mathrm{T}} = \begin{bmatrix} P - P_{\mathrm{S}} & \omega - \omega_{\mathrm{S}} \end{bmatrix}^{\mathrm{T}} \tag{2}$$

where ω is the local angular frequency of the inverter, and P is the active power of the inverter.

Besides, in the ac power grid, based on the power transmission characteristics of inductive transmission lines [32], the relationship between the active power P and the power angle δ is

$$P = \frac{EU}{X}\sin\delta = \frac{EU}{X}\delta + O(\delta^3) = P_{\mathrm{m}}\delta + O(\delta^3) \tag{3}$$

where E is the output voltage of the inverter, U is the voltage of the power grid, X is the impedance between the inverter and the grid, P_{m} is the maximum active power transmission limit, and $O(\delta^3)$ is the high-order term of δ.

Generally, the power angle is small enough and $O(\delta^3)$ can be ignored. Taking the derivative of (3), it is obtained that

$$\Delta\dot{P} = \dot{P} = P_{\mathrm{m}}\dot{\delta} = P_{\mathrm{m}}\Delta\omega. \tag{4}$$

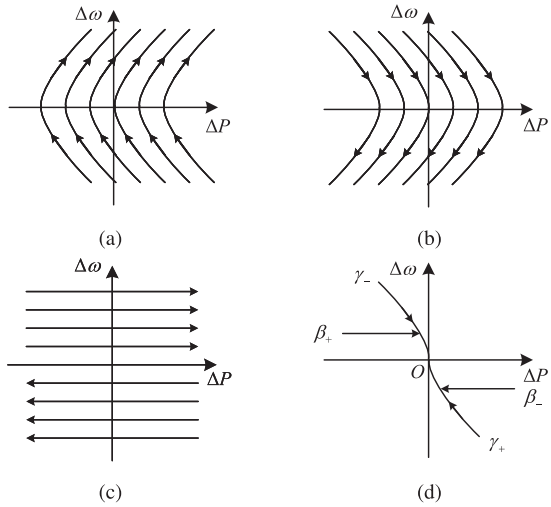

Fig. 2. Phase trajectory diagram. (a) u is $u_{\max}$. (b) u is $-u_{\max}$. (c) u is 0. (d) Four special phase trajectories.

Therefore, in the time interval (t_0, t_{S}), the standard state-space function of the frequency characteristic is

$$\dot{\mathbf{x}} = \mathbf{A}\mathbf{x} + \mathbf{B}u \tag{5}$$

$$\mathbf{A} = \begin{bmatrix} 0 & P_{\mathrm{m}} \\ 0 & 0 \end{bmatrix},\ \mathbf{B} = \begin{bmatrix} 0 \\ 1 \end{bmatrix} \tag{6}$$

where u is the control quantity.

In the proposed model, the initial state $\mathbf{x}(t_0)$ is decided by the changed values of P_0 and ω_{g}. Besides, the target of the proposed control is to make the actual values of state variables equal to their steady-state values without the steady-state error. Therefore, the final state $\mathbf{x}(t_{\mathrm{S}})$ should be 0. They can be expressed as

$$\begin{cases} \mathbf{x}(t_0) = \begin{bmatrix} -\Delta P_0 + k_{\mathrm{p}}\Delta\omega_{\mathrm{g}} & -\Delta\omega_{\mathrm{g}} \end{bmatrix}^{\mathrm{T}} \\ \mathbf{x}(t_{\mathrm{S}}) = \mathbf{0} \end{cases} \tag{7}$$

where t_0 is the initial time point, ΔP_0 is the changed value of P_0, and $\Delta\omega_{\mathrm{g}}$ is the changed value of ω_{g}.

B. Phase Trajectory Analysis

The proposed control is obtained by analyzing the phase trajectory of the standard state-space model. As a basic mathematical tool, the detailed principle of the phase trajectory analysis can be found in most textbooks of the modern control theory, such as textbooks [33], [34]. The phase trajectory analysis requires obtaining a phase plane first. As shown in Fig. 2, a plane is obtained by choosing state variables ΔP and $\Delta\omega$ as the abscissa and ordinate, namely the phase plane. The phase plane assigns a coordinate to each point, representing a state of the state vector. For example, the state vector corresponding to the point (x_{10}, x_{20}) is

$$\mathbf{x} = \begin{bmatrix} x_{10} & x_{20} \end{bmatrix}^{\mathrm{T}}. \tag{8}$$

The solution of the two-order state-space equation in (5) is

$$\mathbf{x} = \begin{bmatrix} \Delta P_{\text{ini}} + P_{\text{m}} \int_0^t \left(\Delta\omega_{\text{ini}} + \int_0^t u dt \right) dt \\ \Delta\omega_{\text{ini}} + \int_0^t u dt \end{bmatrix} \tag{9}$$

where ΔP_{ini} and $\Delta\omega_{\text{ini}}$ are the initial values of ΔP and $\Delta\omega$.

As shown in (5) and (6), the control quantity u is just equal to the RoCoF of the inverter

$$u = \Delta\dot{\omega} = \dot{\omega} = \text{RoCoF}. \tag{10}$$

When the control quantity u is equal to the positive maximum RoCoF limit $u_{\max}$, negative maximum RoCoF limit $-u_{\max}$, and 0, the solution in (9) can be expressed as

$$\mathbf{x} = \begin{cases} \begin{bmatrix} \Delta P_{\text{ini}} + P_{\text{m}} \left(\Delta\omega_{\text{ini}} t + 0.5 u_{\max} t^2 \right) \\ \Delta\omega_{\text{ini}} + u_{\max} t \end{bmatrix}, & u = u_{\max} \\ \begin{bmatrix} \Delta P_{\text{ini}} + P_{\text{m}} \left(\Delta\omega_{\text{ini}} t - 0.5 u_{\max} t^2 \right) \\ \Delta\omega_{\text{ini}} - u_{\max} t \end{bmatrix}, & u = -u_{\max} \\ \begin{bmatrix} \Delta P_{\text{ini}} + P_{\text{m}} \Delta\omega_{\text{ini}} t \\ \Delta\omega_{\text{ini}} \end{bmatrix}, & u = 0. \end{cases} \tag{11}$$

As shown in (11), when ΔP_{ini}, $\Delta\omega_{\text{ini}}$, P_{m}, and $u_{\max}$ are constant, the state vector varies by the time variable t. In the phase plane, each point represents a state of the state vector. Therefore, these varying state vectors in (11) can be represented by a line, namely phase trajectory. And an arrow represents the changing direction of the state vector as time increases. As shown in Fig. 2(a)–(c), when the control quantity u is $u_{\max}$, $-u_{\max}$, and 0, the corresponding phase trajectories are signed as l_+, l_-, and l_0. The functions of these lines can be obtained by eliminating the time variable t in (11), which are

$$\begin{cases} l_+ = \left\{ (\Delta P, \Delta\omega) | \Delta P = \Delta P_{\text{ini}} + K(\Delta\omega^2 - \Delta\omega_{\text{ini}}^2) \right\} \\ l_- = \left\{ (\Delta P, \Delta\omega) | \Delta P = \Delta P_{\text{ini}} - K(\Delta\omega^2 - \Delta\omega_{\text{ini}}^2) \right\} \\ l_0 = \left\{ (\Delta P, \Delta\omega) | \Delta\omega = \Delta\omega_{\text{ini}} \right\} \end{cases} \tag{12}$$

where K is the form factor decided by P_{m} and $u_{\max}$

$$K = 0.5 P_{\text{m}} u_{\max}^{-1}. \tag{13}$$

As shown in (12), when u is $u_{\max}$ and $-u_{\max}$, the phase trajectories are parabolas. In (11), when u is $u_{\max}$, $\Delta\omega$ increases when the time increases and the arrow goes up. When u is $-u_{\max}$, $\Delta\omega$ decreases when the time increases and the arrow goes down. When u is 0, the phase trajectories are lines parallel to the horizontal axis. In (11), when $\Delta\omega_{\text{ini}}$ is positive, ΔP increases when the time increases and the arrow goes right. When $\Delta\omega_{\text{ini}}$ is negative, ΔP decreases when the time increases and the arrow goes left. Besides, with different initial values, the exact functions in (12) are different. Therefore, l_+ represents a series of phase trajectories with the same shape but different intercepts. The same applies to l_- and l_0.

C. Proposed Control

As shown in Fig. 2(a)–(c), the different values of the control quantity lead to different phase trajectories. For each value of the control quantity alone, the phase trajectory points to the infinite.

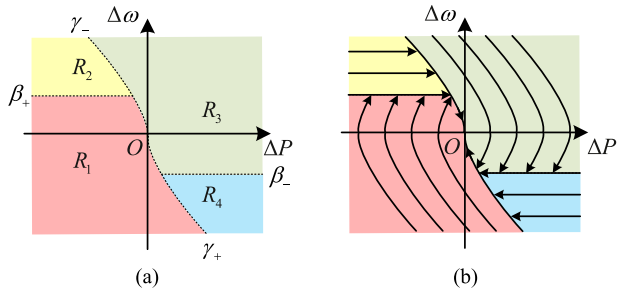

Fig. 3. Coordinate plane partition and the phase trajectory of the proposed control. (a) Coordinate plane partition. (b) Phase trajectory of the proposed control.

And the state vector cannot be controlled to be their set steady values. However, by switching the value of the control quantity properly, with the combination of different phase trajectories, the state vector can be transferred to the origin of coordinates quickly and stably. This is the main idea of the proposed switched active power control.

To achieve the aforementioned objective, four special phase trajectories are used as the boundary, which include γ_+, γ_-, β_+, and β_- shown in Fig. 2(d). In l_+ and l_-, phase trajectories through the origin of coordinates are labeled as γ_+ and γ_-. In l_0, phase trajectories through points $(0, \pm\Delta\omega_{\max})$ are labeled as β_+ and β_-, where $\Delta\omega_{\max}$ is the maximum frequency overshoot limit. And functions of the four boundaries are

$$\begin{cases} \gamma_+ = \left\{ (\Delta P, \Delta\omega) | \Delta P = K\Delta\omega^2,\ \Delta\omega < 0 \right\} \\ \gamma_- = \left\{ (\Delta P, \Delta\omega) | \Delta P = -K\Delta\omega^2,\ \Delta\omega > 0 \right\} \\ \beta_+ = \left\{ (\Delta P, \Delta\omega) | \Delta\omega = \Delta\omega_{\max},\ \Delta P < -K\Delta\omega^2 \right\} \\ \beta_- = \left\{ (\Delta P, \Delta\omega) | \Delta\omega = -\Delta\omega_{\max},\ \Delta P > K\Delta\omega^2 \right\} \end{cases} . \tag{14}$$

As shown in Fig. 3, the four boundaries divide the coordinate plane into four parts signed by R_1, R_2, R_3, and R_4

$$\begin{cases} R_1 = \left\{ (\Delta P, \Delta\omega) | \Delta P \le -K\Delta\omega \left| \Delta\omega \right|, \Delta\omega < \Delta\omega_{\max} \right\} \\ R_2 = \left\{ (\Delta P, \Delta\omega) | \Delta P < -K\Delta\omega \left| \Delta\omega \right|, \Delta\omega \ge \Delta\omega_{\max} \right\} \\ R_3 = \left\{ (\Delta P, \Delta\omega) | \Delta P \ge -K\Delta\omega \left| \Delta\omega \right|, \Delta\omega > -\Delta\omega_{\max} \right\} \\ R_4 = \left\{ (\Delta P, \Delta\omega) | \Delta P > -K\Delta\omega \left| \Delta\omega \right|, \Delta\omega \le -\Delta\omega_{\max} \right\} \end{cases} . \tag{15}$$

And the proposed switched active power control can be obtained by setting the different values of the control quantity u for the state vector belonging to different parts in (15), whose control law u_{P} is

$$u_{\text{P}} = \begin{cases} u_{\max}, & \mathbf{x} \in R_1 \\ -u_{\max}, & \mathbf{x} \in R_3 \\ 0, & \text{otherwise} \end{cases} . \tag{16}$$

And the control loop of the proposed active power control is shown in Fig. 4.

For the state vector with different initial states, the proposed control can transfer the state vector to the origin of coordinates. As shown in Fig. 5, there are six different cases. As the cases

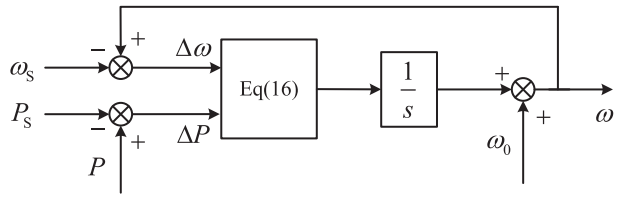

Fig. 4. Control loop of the proposed active power control.

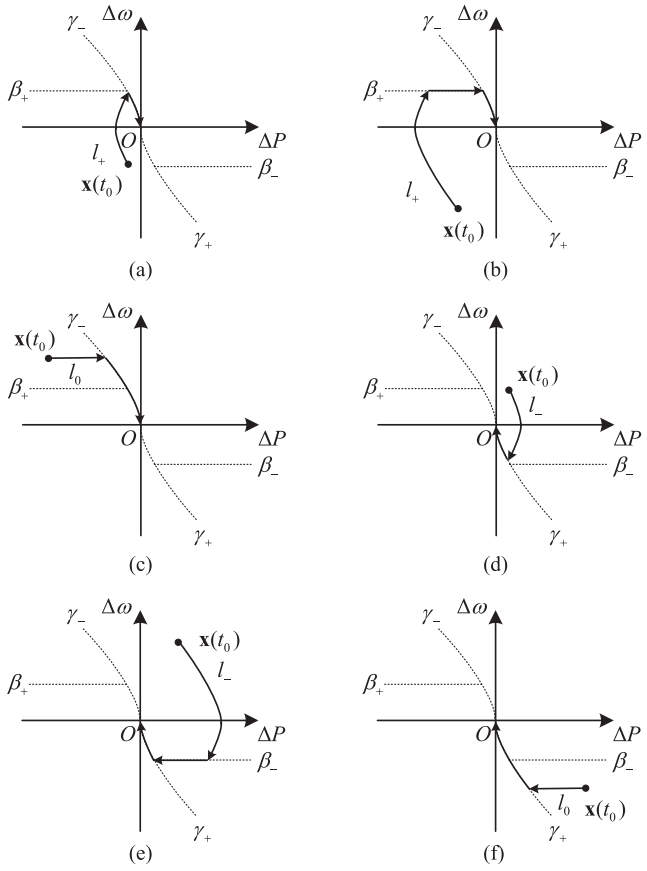

Fig. 5. Phase trajectory of the state vector with different initial states. (a) $\mathbf{x}(t_0) \in R_1$ (case 1). (b) $\mathbf{x}(t_0) \in R_1$ (case 2). (c) $\mathbf{x}(t_0) \in R_2$. (d) $\mathbf{x}(t_0) \in R_3$ (case 1). (e) $\mathbf{x}(t_0) \in R_3$ (case 2). (f) $\mathbf{x}(t_0) \in R_4$.

shown in Fig. 5(d)–(f) are symmetrical to the cases shown in Fig. 5(a)–(c), only the first three cases are discussed here.

1) For $\mathbf{x}(t_0) \in R_1$, the state vector follows a phase trajectory in l_+ with u set to $u_{\max}$ first. If $\Delta\omega_{\max}$ is large enough, the aforementioned phase trajectory is only intersected with the boundary γ_-. After the intersection, u switches to $-u_{\max}$, and the state vector continues along the phase trajectory γ_- toward the origin of coordinates. Therefore, the total transfer trajectory is $l_+ \to \gamma_- \to O$.
2) For $\mathbf{x}(t_0) \in R_1$, if $\Delta\omega_{\max}$ is relatively small, the phase trajectory intersects with boundary β_+ before intersecting with γ_-. After this intersection, u switches to 0 and the state vector continues along the phase trajectory β_+ toward the intersection between β_+ and γ_-. Finally, after the intersection between β_+ and γ_-, u switches to $-u_{\max}$, and the state vector continues along the phase trajectory γ_- toward the origin of coordinates. Therefore, the total transfer trajectory is $l_+ \to \beta_+ \to \gamma_- \to O$.
3) For $\mathbf{x}(t_0) \in R_2$, the state vector follows a phase trajectory in l_0 with u set to 0 first. Then, after the intersection between l_0 and γ_-, u switches into $-u_{\max}$, and the state vector continues along the phase trajectory γ_- toward the origin of the coordinate. Therefore, the total transfer trajectory is $l_0 \to \gamma_- \to O$.

In the aforementioned processes, the maximum RoCoF is $u_{\max}$, and the maximum frequency overshoot is $\Delta\omega_{\max}$. They can be adjusted directly, which enhances the frequency stability.

As a switched control, there is a buffeting problem when the inverter is close to the steady state. Therefore, the proposed controller is only triggered for large disturbances. When the inverter is close to the steady state, the control law returns to the VSG control law and the final control law is

$$u = \begin{cases} -\frac{1}{J\omega_0}\Delta P - \frac{D+k_p}{J\omega_0}\Delta\omega, & \|\mathbf{x}\| \le \varepsilon \\ u_P, & \|\mathbf{x}\| > \varepsilon \end{cases} \tag{17}$$

where ε is the threshold value to decide whether the inverter is at a steady state, and J and D are the inertia and damping of the VSG control.

As the VSG control is only used when the inverter is close to the steady state, it does not influence the following calculation and comparison.

D. Stability Analysis of the Proposed Control

The stability analyses include small-signal analyses and large-signal analyses. As shown in (17), the proposed control is switched into the VSG control when the converter is at a steady state. The small-signal analysis of the proposed control is the same as the VSG control, which can be found in [35] and [36], thus not repeated here.

The large-signal stability of the proposed control is analyzed with the Lyapunov function. The Lyapunov function $V(\mathbf{x})$ is a positive-definite continuous function, with its derivative $dV(\mathbf{x})/dt$ being negative semidefinite but not equal to zero for all $\mathbf{x} \neq 0$. Based on the Lyapunov theorem of stability, if the Lyapunov function can be found, the system is asymptotically stable. Especially, when $\|\mathbf{x}\|$ tends to ∞, if the Lyapunov function $V(\mathbf{x})$ tends to ∞ simultaneously, the system is global asymptotically stable.

For the proposed control, the Lyapunov function $V(\mathbf{x})$ is

$$V(\mathbf{x}) = \begin{cases} K\Delta\omega^2 + \Delta P, & \Delta P \ge 0 \\ K\Delta\omega^2 - \Delta P, & \Delta P < 0 \end{cases}. \tag{18}$$

As shown in in the aforementioned equation, $V(\mathbf{x})$ is a positive-definite continuous function. And when $\|\mathbf{x}\|$ tends to ∞, the Lyapunov function $V(\mathbf{x})$ tends to ∞ simultaneously.

Then, it is shown that its derivative $dV(\mathbf{x})/dt$ is negative semidefinite but not equal to zero for all $\mathbf{x} \neq 0$. The derivative of $V(\mathbf{x})$ in (18) is

$$\frac{dV(\mathbf{x})}{dt} = \begin{cases} \frac{P_m}{u_{\max}}\Delta\omega\frac{d\Delta\omega}{dt} + \frac{d\Delta P}{dt}, & \Delta P \ge 0 \\ \frac{P_m}{u_{\max}}\Delta\omega\frac{d\Delta\omega}{dt} - \frac{d\Delta P}{dt}, & \Delta P < 0 \end{cases}. \tag{19}$$

Substituting (5) and (6) into (19) and eliminating $d\Delta P/dt$ and $d\Delta\omega/dt$, the derivative is

$$\frac{dV(\mathbf{x})}{dt} = \begin{cases} P_{\mathrm{m}}\Delta\omega(u/u_{\max}+1), & \Delta P \geq 0 \\ P_{\mathrm{m}}\Delta\omega(u/u_{\max}-1), & \Delta P < 0 \end{cases}. \tag{20}$$

Substituting the proposed control in (16) into (20), the derivative is

$$\frac{dV(\mathbf{x})}{dt} = \begin{cases} 2P_{\mathrm{m}}\Delta\omega, & \mathbf{x} \in R_1 \text{ and } \Delta P \geq 0 \\ 0, & \mathbf{x} \in R_1 \text{ and } \Delta P < 0 \\ -P_{\mathrm{m}}\Delta\omega, & \mathbf{x} \in R_2 \\ -2P_{\mathrm{m}}\Delta\omega, & \mathbf{x} \in R_3 \text{ and } \Delta P < 0 \\ 0, & \mathbf{x} \in R_3 \text{ and } \Delta P \geq 0 \\ P_{\mathrm{m}}\Delta\omega, & \mathbf{x} \in R_4 \end{cases}. \tag{21}$$

In the aforementioned equation, the derivative is decided by the value of $\Delta\omega$. As shown in Fig. 3, in the four parts where $dV(\mathbf{x})/dt$ is not equal to 0, the value of $\Delta\omega$ is

$$\begin{cases} \Delta\omega \leq 0, & \mathbf{x} \in R_1 \text{ and } \Delta P \geq 0 \\ \Delta\omega > 0, & \mathbf{x} \in R_2 \\ \Delta\omega > 0, & \mathbf{x} \in R_3 \text{ and } \Delta P < 0 \\ \Delta\omega < 0, & \mathbf{x} \in R_4 \end{cases}. \tag{22}$$

Substituting (22) into (21), the derivative $dV(\mathbf{x})/dt$ is negative semidefinite. Besides, for $\mathbf{x} \neq 0$, $dV(\mathbf{x})/dt$ is not always equal to 0. Therefore, based on the Lyapunov theorem of stability, for the active power control loop, the inverter with the proposed switched active power control is global asymptotically stable.

III. Control Design

In this section, parameters of the proposed control are designed, which include the maximum RoCoF limit $u_{\max}$ and the maximum frequency overshoot limit $\Delta\omega_{\max}$. Due to the clear physical meaning of the proposed control, these parameters can be designed by analytical equations directly.

A. Maximum RoCoF Limit

A smaller $u_{\max}$ is better for frequency stability. However, a small $u_{\max}$ will lead to a large active power overshoot of the inverter. As the maximum power is limited by the hardware of the inverter, $u_{\max}$ should be designed accordingly.

When there are step changes for the active power reference P_0, the initial state of the state vector is

$$\mathbf{x}(t_0) = \begin{bmatrix} -\Delta P_0 & 0 \end{bmatrix}^{\mathrm{T}}. \tag{23}$$

When $\Delta P_0 > 0$, $\mathbf{x}(t_0)$ is on the negative half of the abscissa axis and $\mathbf{x}(t_0) \in R_1$. As shown in Fig. 6, when the state vector is transferred to the origin of coordinates, the absolute value of ΔP is monotone decreasing and there is no overshoot. When $\Delta P_0 < 0$, the same conclusion can be obtained with symmetric processes, which is not expanded here.

When there are step changes for power grid frequency ω_{g}, the initial state of the state vector is

$$\mathbf{x}(t_0) = \begin{bmatrix} k_{\mathrm{p}}\Delta\omega_{\mathrm{g}} & -\Delta\omega_{\mathrm{g}} \end{bmatrix}^{\mathrm{T}}. \tag{24}$$

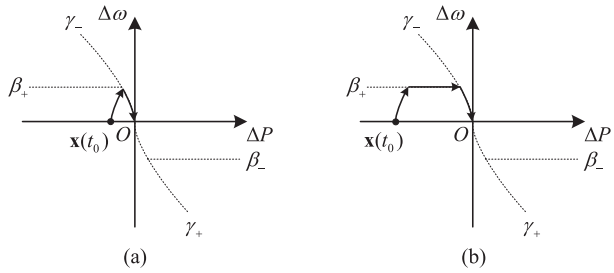

Fig. 6. Phase trajectory of the state vector with the active power reference increase. (a) $\mathbf{x}(t_0) \in R_1$ (case 1). (b) $\mathbf{x}(t_0) \in R_1$ (case 2).

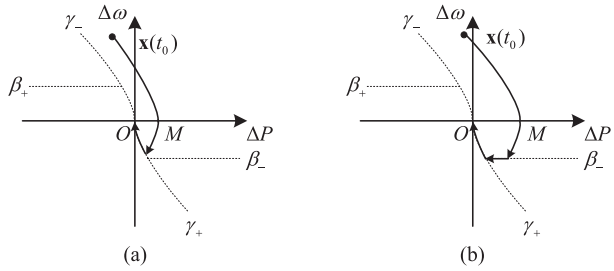

Fig. 7. Phase trajectory of the state vector with the grid frequency decrease and active power overshoot. (a) $\mathbf{x}(t_0) \in R_3$ (case 1). (b) $\mathbf{x}(t_0) \in R_3$ (case 2).

When $\Delta\omega_{\mathrm{g}} < 0$, $\mathbf{x}(t_0)$ is in the second quadrant. As shown in Fig. 5(a)–(c), in the second quadrant, when $\mathbf{x}(t_0) \in R_1$ or $\mathbf{x}(t_0) \in R_2$, the absolute value of ΔP is monotone decreasing in the whole process and there is no active power overshoot. As shown in Fig. 7, when $\mathbf{x}(t_0) \in R_3$, the maximum overshoot occurs at point M, where M is the intersection between the abscissa axis and phase trajectory. Substituting (24) into (12), the point M is

$$M : ((K\Delta\omega_{\mathrm{g}} + k_{\mathrm{p}})\Delta\omega_{\mathrm{g}}, 0). \tag{25}$$

Considering the condition of $\mathbf{x}(t_0) \in R_3$, the maximum overshoot ΔP_{ov} is

$$\Delta P_{\mathrm{ov}} = (K\Delta\omega_{\mathrm{g}} + k_{\mathrm{p}})\Delta\omega_{\mathrm{g}}, \quad k_{\mathrm{p}} < -K\Delta\omega_{\mathrm{g}}. \tag{26}$$

When $\Delta\omega_{\mathrm{g}} > 0$, with symmetric processes, ΔP_{ov} can be obtained and expressed as the following unified form:

$$\Delta P_{\mathrm{ov}} = \begin{cases} (0.5P_{\mathrm{m}}u_{\max}^{-1}\,|\Delta\omega_{\mathrm{g}}| - k_{\mathrm{p}})\,|\Delta\omega_{\mathrm{g}}|, & |\Delta\omega_{\mathrm{g}}| > k_{\mathrm{p}}/K \\ 0, & |\Delta\omega_{\mathrm{g}}| \leq k_{\mathrm{p}}/K \end{cases}. \tag{27}$$

This overshoot is obtained with the assumption that $\sin\delta \approx \delta$. And the exact maximum active power $P_{\max}$ is calculated without this assumption

$$\frac{P_{\max}}{P_{\mathrm{m}}} = \sin\left(\frac{P_{\mathrm{S}} + \Delta P_{\mathrm{ov}}}{P_{\mathrm{m}}}\right), \quad |\Delta\omega_{\mathrm{g}}| > k_{\mathrm{p}}/K. \tag{28}$$

Therefore, to meet the active power output limit $P_{\max}$, $u_{\max}$ is

$$u_{\max} \geq \frac{0.5P_{\mathrm{m}}\Delta\omega_{\mathrm{gmax}}^2}{P_{\mathrm{m}}\arcsin(P_{\max}/P_{\mathrm{m}}) - P_{\mathrm{S}} + k_{\mathrm{p}}|\Delta\omega_{\mathrm{gmax}}|} \tag{29}$$

where $\Delta\omega_{\mathrm{gmax}}$ is the maximum step change of ω_{g}.

In (29), $P_{\max}$ is the active power output limit. In a grid-connect inverter, the total output current is the sum of active power

current and reactive power current. The active power output limit can be obtained by the total current limit $I_{\max}$ and the maximum reactive power output limit $Q_{\max}$ of the inverter

$$P_{\max} = \sqrt{(EI_{\max})^2 - Q_{\max}^2}. \tag{30}$$

B. Maximum Frequency Overshoot Limit

A smaller $\Delta\omega_{\max}$ is better for frequency stability. However, a small $\Delta\omega_{\max}$ will lead to a large response time t_S. When $\Delta\omega_{\max}$ is set to 0, the maximum t_S is $+\infty$, which is unacceptable. Therefore, it is important to set a proper $\Delta\omega_{\max}$ to keep a balance between frequency overshoot and response time.

With a small $\Delta\omega_{\max}$, β_+ and β_- are approximately coincided with the abscissa axis, and the maximum response time occurs in Figs. 6(b) and 7(b).

When there is a step change for the active power reference P_0, the initial state of the state vector is (23). As shown in Fig. 6(b), when $\Delta P_0 > 0$, the phase trajectory is $l_+ \to \beta_+ \to \gamma_- \to O$. With a small $\Delta\omega_{\max}$, β_+ is approximately coincided with the abscissa axis. Therefore, processes $l_+ \to \beta_+$ and $\gamma_- \to O$ are much shorter than the process $\beta_+ \to \gamma_-$. And the total response time is mainly decided by the time of the process $\beta_+ \to \gamma_-$, where the state vector moves following the x-direction and the controlled quantity is 0. Based on the proposed model in (5) and (6), the move speed of the state vector is

$$\frac{d\Delta P}{dt} = \Delta\omega_{\max} P_m. \tag{31}$$

Besides, as processes $l_+ \to \beta_+$ and $\gamma_- \to O$ are short enough to be ignored, the total move distance can be seen as ΔP_0 approximately. Therefore, the total response time is

$$t_S = \frac{|\Delta P_0|}{\Delta\omega_{\max} P_m} + O(\Delta\omega_{\max}) \tag{32}$$

where $O(\Delta\omega_{\max})$ is the high-order term of $\Delta\omega_{\max}$ and represents the ignored time in processes $l_+ \to \beta_+$ and $\gamma_- \to O$.

When $\Delta P_0 < 0$, with a symmetric process, the same result can be obtained, which is not repeated here.

When there is a step change for the power grid frequency ω_g, the initial state of the state vector is (24). When $\omega_g < 0$, as shown in Fig. 7(b), the whole phase trajectory can be divided into two parts. In the first part, the state vector is transferred from the initial state to point M. In this part, the ordinate is reduced from $\Delta\omega_g$ to 0. Based on the proposed model, $d\omega_g/dt$ is equal to the control quantity u, which is equal to $-u_{\max}$ in this process. Therefore, the time of the first part is $|\Delta\omega_g|/u_{\max}$. In the second part, the state vector is transferred from point M to the origin of the coordinates. As shown in Fig. 7(b), this process is similar to the process in Fig. 6(b). The only difference is that the initial abscissa is $K\Delta\omega_g^2 - k_p|\Delta\omega_g|$ in (25) rather than ΔP_0. Therefore, the time of the second part is $(K\Delta\omega_g^2 - k_p|\Delta\omega_g|)/(\Delta\omega_{\max} P_m)$, and the total response time is

$$t_S = \frac{|\Delta\omega_g|}{u_{\max}} + \frac{K\Delta\omega_g^2 - k_p|\Delta\omega_g|}{\Delta\omega_{\max} P_m} + O(\Delta\omega_{\max}). \tag{33}$$

When $\Delta\omega_g > 0$, with a symmetric process, the same result can be obtained, which is not repeated here.

Therefore, for the primary frequency control, $\Delta\omega_{\max}$ is

$$\Delta\omega_{\max} \geq \frac{u_{\max}(K\Delta\omega_{gmax}^2) - k_p|\Delta\omega_{gmax}|}{P_m(u_{\max} t_{Smax} - |\Delta\omega_{gmax}|)}. \tag{34}$$

For the secondary frequency control and active power reference changes, $\Delta\omega_{\max}$ is

$$\Delta\omega_{\max} \geq \frac{|\Delta P_{0max}|}{P_m t_{Smax}} \tag{35}$$

where t_{Smax} is the maximum allowable response time of the primary and secondary frequency control, and ΔP_{0max} is the maximum step change of P_0.

IV. Comparison

In this section, the proposed control is compared with the original VSG control [23] and other similar controls proposed in recent years, which include the high-order linear control [25], self-adaptive VSG control [28], fractional-order VSG control [30], and H_∞ control [31].

The comparison can be divided into two steps. In the first step, it is shown that the selected controls can be expressed by the proposed state-space model with special control laws. In this way, regardless of the specific details of these controls, they can be analyzed using the same approach. In the second step, it is proven that for all controls that can be expressed by the proposed model, the proposed active power control has the lowest RoCoF and frequency overshoot. As the existing controls can be expressed by the proposed model and their control laws are different from the proposed control law, the proposed control has lower RoCoF and frequency overshoot than existing controls. The detailed comparisons are shown as follows.

A. Relationship Among Different Controls

First, with the standard state-space model, the aforementioned controls can be expressed as following unified forms:

$$\begin{cases} \dot{\mathbf{x}} = \mathbf{A}\mathbf{x} + \mathbf{B}u \\ u = f(\Delta P, \Delta\omega, t) \end{cases} \tag{36}$$

where $f(\Delta P, \Delta\omega, t)$ is decided by the control method.

The detailed derivation of (36) is shown in the Appendix.

B. Comparison of Maximum RoCoF

Next, the RoCoF is discussed, which is limited by the maximum power $P_{\max}$ of the inverter. When the frequency of the power grid decreases, based on the standard state-space model in (5), (6), and (36), the relationship between P and $\Delta\omega$ is

$$P = P_0 + P_m \int \Delta\omega dt. \tag{37}$$

As shown in Fig. 8(a), the output power is maximum at time point t_1. And the maximum output power $P_{\max}$ is positive to the blue shadow area in the time interval (t_0, t_1)

$$P_{\max} = P_0 + P_m \int_{t_0}^{t_1} \Delta\omega dt. \tag{38}$$

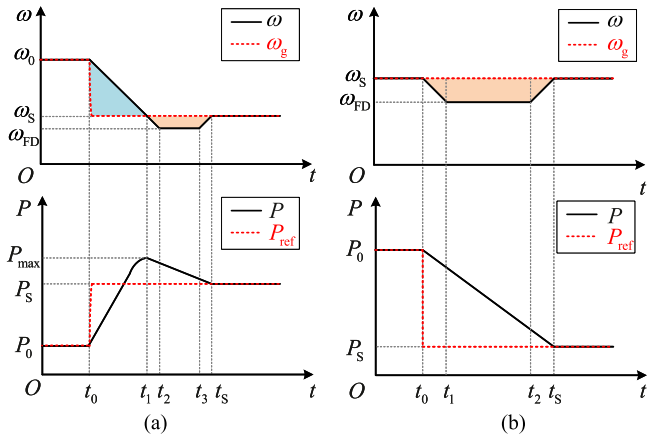

Fig. 8. Waveform of the active power and frequency of the inverter. (a) Grid frequency decreases. (b) Active power reference decreases.

As shown in Fig. 8(a), to decrease the blue shadow area, ω should decrease as quickly as possible. As analyzed in (10), in this case, ω in the proposed control is

$$\omega = \omega_0 - u_{\max} t. \tag{39}$$

As ω in the proposed control always decreases with the maximum RoCoF limit $u_{\max}$, ω in the other controls cannot decrease faster than the proposed control. Therefore, with the same maximum RoCoF limit, the maximum output power $P_{\max}$ of the other controls is higher than the proposed control. That is to say, when $P_{\max}$ is limited by the hardware of the inverter, the lowest $u_{\max}$ can be set in the proposed control and the maximum RoCoF of the proposed control is lowest as well.

C. Comparison of Frequency Overshoot

Then, the frequency overshoot is discussed, which is limited by the response time. As shown in Fig. 8(a), in the time interval (t_1, t_S), the active power P is reduced from $P_{\max}$ to P_S. Based on the standard state-space model in (5), (6), and (36), $P_{\max} - P_S$ is positive to the orange shadow area in the time interval (t_1, t_S). As the time intervals (t_1, t_2) and (t_3, t_S) are much lower than the time interval (t_2, t_3), they can be ignored and

$$|P_{\max} - P_S| \approx P_m \int_{t_2}^{t_3} |\Delta\omega| dt = P_m |\Delta\bar{\omega}| (t_3 - t_2) \tag{40}$$

where $\Delta\bar{\omega}$ is the average value of $\Delta\omega$ between t_2 and t_3.

As shown in (40), when other parameters are fixed, for the fixed response time, $\Delta\bar{\omega}$ is fixed as well. The maximum value $\Delta\omega_{\max}$ cannot be lower than the average value $\Delta\bar{\omega}$, and they are equal to each other only when $\Delta\omega$ is constant. Therefore, to obtain the minimum $\Delta\omega_{\max}$, $\Delta\omega$ should be controlled equal to $\Delta\omega_{\max}$ in the time interval (t_2, t_3). As shown in Fig. 5(b) and (e), ω in the proposed control conforms to the above situation. Therefore, when the maximum response time is limited as $t_{S\max}$, the lowest $\Delta\omega_{\max}$ can be set in the proposed control.

As shown in Fig. 8(b), when the active power reference decreases, the whole process is the same, which is not repeated here.

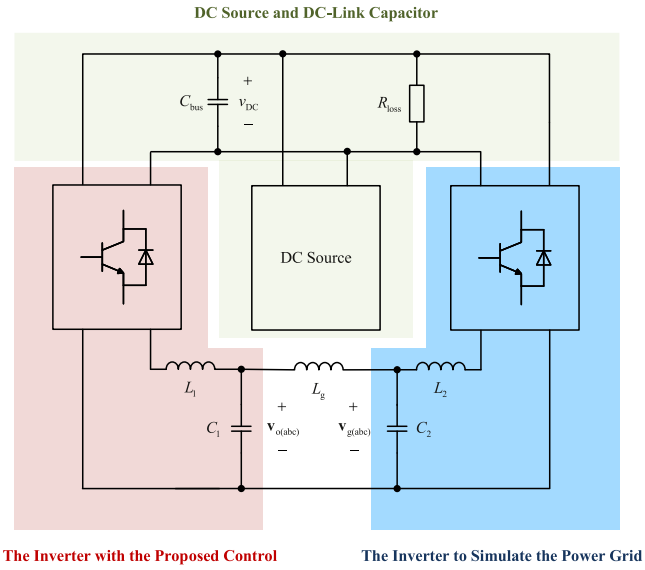

Fig. 9. Main circuit of the experiment.

D. Comparison of the Frequency Nadir

Finally, the frequency nadir is discussed. A low-frequency nadir can lead to the misoperation of the low frequency load shedding device. Therefore, a larger frequency nadir is better for frequency stability.

As shown in Fig. 8, the frequency nadir ω_{FD} is decided by the steady frequency ω_S and the frequency overshoot $\Delta\omega_{\max}$

$$\omega_{FD} = \omega_S - \Delta\omega_{\max}. \tag{41}$$

As discussed in the last subsection, the proposed control has the lowest $\Delta\omega_{\max}$. Therefore, based on (41), the proposed control has the largest frequency nadir.

V. Verification

In this section, the proposed control and the comparison with other controls are verified by simulations and experiments.

A. Verification Setup

In this verification, the tested circuit is the same as the main circuit shown in Fig. 1. As the power level of the grid-connected inverter is generally much lower than the total power grid, the grid-connected inverter can be seen as being connected to an infinite bus. The infinite bus is a network node whose voltage is predetermined and remains constant in magnitude, phase, and frequency under all loading conditions [37]. In the simulation, the grid voltage is generated by a controlled AC voltage source, whose angular frequency is always controlled to be equal to the set value. And the line impedance is simulated by inductors.

In the experiment, the circuit is shown in Fig. 9 and the photo of the text rig is shown in Fig. 10. The experiment rig is mainly constituted by two inverters, three line inductors, a dc source, several dc-link capacitors, an auxiliary power supply, several probes (Tektronix TPP0201, Cybertek P1300, and Cybertek CPA300), an oscilloscope (Tektronix DPO3014), and a computer. As introduced in [38], [39], the power grid is generally

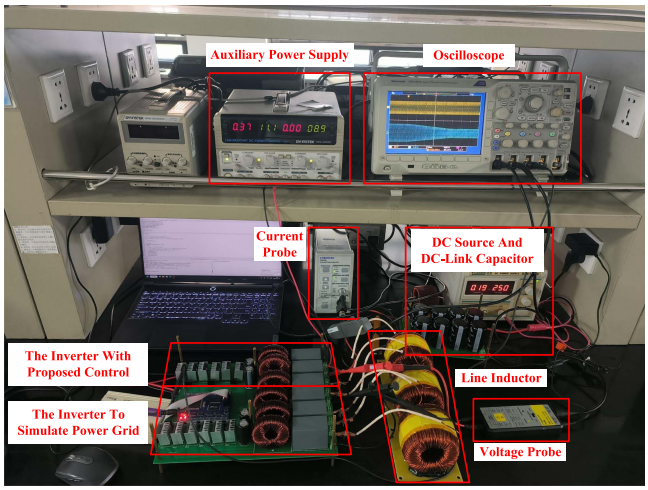

Fig. 10. Photograph of the test rig in the experiment.

TABLE I
PARAMETERS OF VERIFICATIONS

Parameter	Sign	Value	
		Simulation	Experiment
Nominal Angular Frequency	ω_0	100π rad/s	100π rad/s
Active Power Transfer Limit	P_{m}	21 kW	2.1 kW
Droop Coefficient	k_{p}	2 kJ/rad	200 J/rad
Maximum Active Power Limit	P_{max}	5 kW	500 W
Maximum Response Time Limit	t_{Smax}	1 s	1 s
DC-Link Voltage	v_{DC}	800 V	250 V
Grid Line Voltage	v_{rms}	380 V	120 V
Line Inductance	L_{g}	22 mH	22 mH
Inverter Filter Inductance	$L_{1,2}$	3 mH	3 mH
Inverter Filter Capacitance	$C_{1,2}$	20 μF	20 μF
Switching Frequency	f	10 kHz	10 kHz

simulated by an inverter. The same solution is also used in this article, and the power grid is simulated by another three-phase inverter, whose main circuit is the same as that of the tested inverter. The only difference is that the angular frequency of this grid-simulated inverter is locked as the set value, regardless of the input active power. However, the tested inverter is controlled by the proposed control method. Therefore, based on the definition of the infinite bus, for the analysis of the active power control loop, the characteristic of this grid-simulated inverter is the same as the infinite bus in theory.

Besides, in the experiment, the dc-link voltage is maintained by the dc source and dc-link capacitors. Generally, the dc source has no energy feedback function. Therefore, an energy dissipation resistance Rloss is connected to the dc bus, which is 2 kΩ. As the majority of energy is cycled in the experiment rig, the power level of the dc source is permitted to be much lower than the tested power level of the inverter. It will be shown in the following parts of this section that the experiment results fit well with the simulation results, which can prove the validity of this experiment scheme.

The parameters of the verification are listed in Table I. Due to the limitation of experimental conditions, the experiment's power, voltage, and current levels have been proportionally reduced. The ratio of power level between the simulation and experiment is 10:1. Correspondingly, the ratio of voltage and current level between the simulation and experiment are both $\sqrt{10}:1$. This approach ensures that the parameters' per-unit value remains consistent between the simulation and experiment, enabling direct comparison of their respective results.

Except for the aforementioned parameters, in the experiment, the main controller is the digital signal processor TMS320F28335. And a digital-to-analog converter MCP4822 is used to transfer the digital quantities calculated by the main controller into the analog quantities, which include the active power P, angular frequency ω, and RoCoF df/dt of the inverter.

B. Verification of the Proposed Control

On the one hand, the analysis and parameter design of the proposed control are verified by the simulation and experiment of the inverter with the step changes of the grid frequency and the active power reference, and the following cases are analyzed.

Case 1: The grid frequency ω_{g} decreases from 100π rad/s to $100\pi - 0.5$ rad/s, and then, returns to 100π rad/s. The active power reference P_0 is 2 kW in the simulation and 200 W in the experiment.

Case 2: The grid frequency ω_{g} decreases from 100π rad/s to $100\pi - 1$ rad/s, and then, returns to 100π rad/s. The active power reference P_0 is 2 kW in the simulation and 200 W in the experiment.

Case 3: In the simulation, the active power reference P_0 increases from 2 to 4 kW, and then, returns to 2 kW. In the experiment, the active power reference P_0 increases from 200 to 400 W, and then, returns to 200 W. The grid frequency ω_{g} is always 100π rad/s.

Case 4: The grid frequency ω_{g} decreases from 100π rad/s to $100\pi - 0.5$ rad/s, and then, returns to 100π rad/s. The active power reference P_0 is 2.5 kW in the simulation and 250 W in the experiment.

Case 5: The grid frequency ω_{g} decreases from 100π rad/s to $100\pi - 1$ rad/s and then returns to 100π rad/s. The active power reference P_0 is 2.5 kW in the simulation and 250 W in the experiment.

Case 6: In the simulation, the active power reference P_0 increases from 2.5 to 4.5 kW, and then, returns to 2.5 kW. In the experiment, the active power reference P_0 increases from 250 to 450 W, and then, returns to 250 W. The grid frequency ω_{g} is always 100π rad/s.

The allowed active power overshoot is $20\%P_{\mathrm{max}}$ in cases 1–3, and $10\%P_{\mathrm{max}}$ in cases 4–6.

In the above cases, calculated by (29), u_{max} should be larger than 0.548 Hz/s in cases 1–3 and 0.658 Hz/s in cases 4–6, which are set as 0.550 and 0.660 Hz/s, respectively. As calculated by (34) and (35), $\Delta\omega_{\mathrm{max}}$ should be larger than 0.070 rad/s in cases 1 and 2, 0.034 rad/s in cases 4 and 5, and 0.095 rad/s in other cases, which are set as 0.080, 0.040, and 0.120 rad/s, respectively. Besides, to avoid the buffeting problem, as shown in (17), in the aforementioned cases, the control is switched from the proposed control to the VSG control when $|\Delta P| < 0.05P_0$ and $|\Delta\omega| < 0.05\Delta\omega_{\mathrm{max}}$ simultaneously. Correspondingly, when $|\Delta P| > 0.05P_0$ or $|\Delta\omega| > 0.05\Delta\omega_{\mathrm{max}}$, the VSG control is switched to the proposed control.

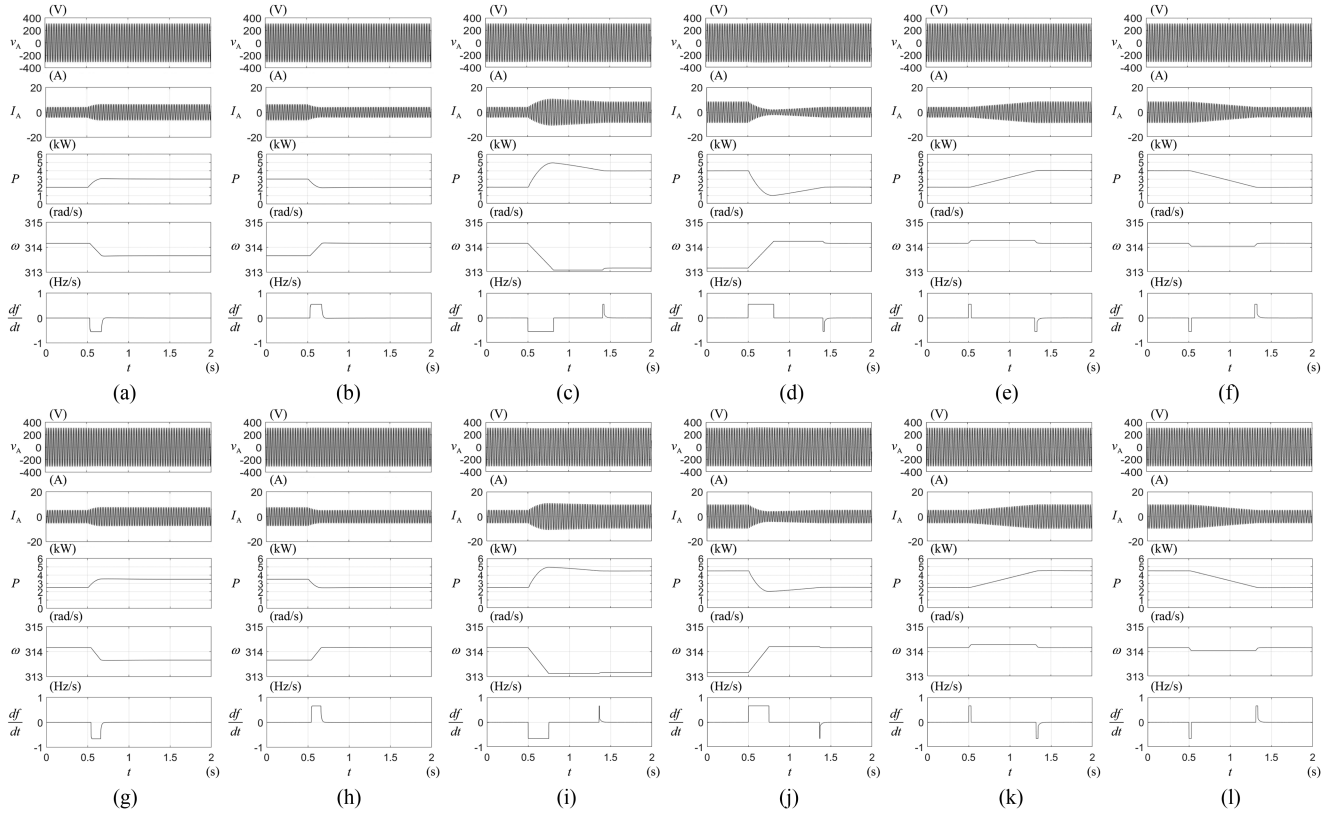

Fig. 11. Simulation waveforms of the proposed control. (a) $\Delta\omega_g$ is -0.5 rad/s (Case 1). (b) $\Delta\omega_g$ is 0.5 rad/s (Case 1). (c) $\Delta\omega_g$ is -1 rad/s (Case 2). (d) $\Delta\omega_g$ is 1 rad/s (Case 2). (e) ΔP_0 is 2 kW (Case 3). (f) ΔP_0 is -2 kW (Case 3). (g) $\Delta\omega_g$ is -0.5 rad/s (Case 4). (h) $\Delta\omega_g$ is 0.5 rad/s (Case 4). (i) $\Delta\omega_g$ is -1 rad/s (Case 5). (j) $\Delta\omega_g$ is 1 rad/s (Case 5). (k) ΔP_0 is 2 kW (Case 6). (l) ΔP_0 is -2 kW (Case 6).

The simulation and experiment waveforms are shown in Figs. 11 and 12. In the experiment, as the change of ω is much smaller than its steady value, when the waveforms of ω are drawn, the base values of ω are set to 312.5 rad/s. Besides, due to the symmetry of the three phases, only the output voltage and current waveforms of one phase are shown.

The simulation and experiment results verify the analysis of the proposed control. First, as shown in Figs. 11 and 12, when the step changes of the grid frequency and active power reference occur, the proposed control can lead the inverter into the new steady state. In the whole process, the maximum RoCoF and frequency overshoot are equal to the given $u_{\max}$ and $\Delta\omega_{\max}$, which verifies the analyses of the proposed control in Section II. Then, for the step changes of the active power reference, there is no overshoot of the active power. For the step changes of the grid frequency, when $|\Delta\omega_g|$ is 0.5 rad/s and lower than k_p/K (0.658 rad/s in cases 1–3 and 0.785 rad/s in cases 4–6), there is no overshoot of the active power and frequency. When $|\Delta\omega_g|$ is 1 rad/s and higher than k_p/K, the maximum active power is just lower than 5 kW in the simulation and 500 W in the experiment, which is the same as the maximum active power limit in Table I. Simulation and experiment results verify the parameter design of $u_{\max}$ in Section III. Finally, the response time of the inverter is always lower than t_{Smax} in Table I. The parameter design of $\Delta\omega_{\max}$ in Section III is also verified by simulation and experiment results.

C. Verification of the Comparison

On the other hand, the comparison with other controls is verified by the simulation and experiment, which includes the simulation and experiment of the inverter with the step decreases of the grid frequency and the active power reference. There are four situations.

Situation 1: The grid frequency ω_g decreases from 100π rad/s to $100\pi - 1$ rad/s. The active power reference P_0 is 2 kW in the simulation and 200 W in the experiment.

Situation 2: In the simulation, the active power reference P_0 decreases from 4 to 2 kW. In the experiment, the active power reference P_0 decreases from 400 to 200 W. The grid frequency ω_g is always 100π rad/s.

Situation 3: The grid frequency ω_g decreases from 100π rad/s to $100\pi - 1$ rad/s. The active power reference P_0 is 2.5 kW in the simulation and 250 W in the experiment.

Situation 4: In the simulation, the active power reference P_0 decreases from 4.5 to 2.5 kW. In the experiment, the active power reference P_0 decreases from 450 to 250 W. The grid frequency ω_g is always 100π rad/s.

To make a fair comparison, the parameters of other controls are designed to meet the maximum active power limit and maximum response time limit in Table I as well. And their RoCoF and frequency overshoot are compared under these conditions. The detailed principle of the parameters design can be found in

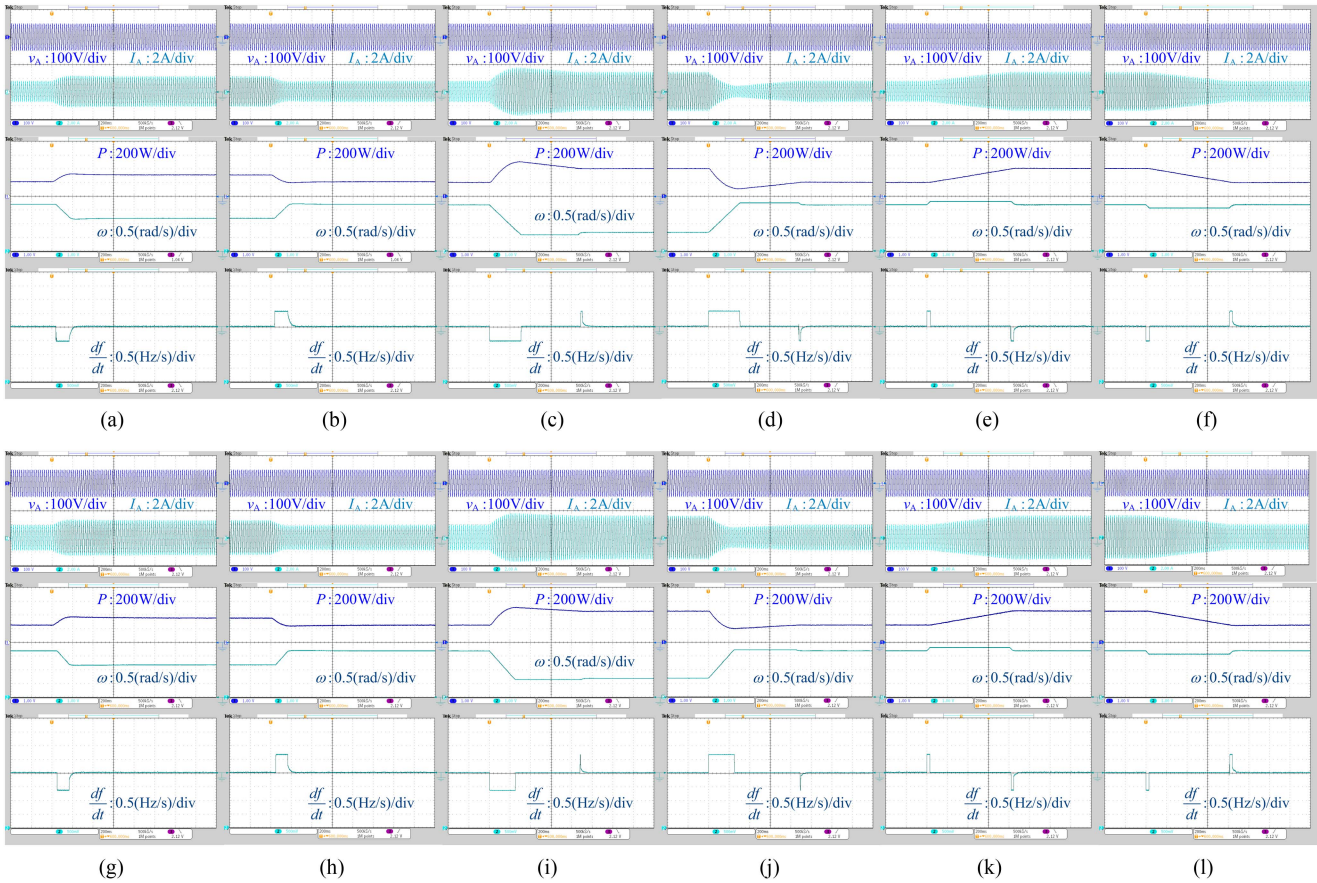

Fig. 12. Experiment waveforms of the proposed control. (a) $\Delta\omega_g$ is -0.5 rad/s (Case 1). (b) $\Delta\omega_g$ is 0.5 rad/s (Case 1). (c) $\Delta\omega_g$ is -1 rad/s (Case 2). (d) $\Delta\omega_g$ is 1 rad/s (Case 2). (e) ΔP_0 is 200 W (Case 3). (f) ΔP_0 is -200W (Case 3). (g) $\Delta\omega_g$ is -0.5 rad/s (Case 4). (h) $\Delta\omega_g$ is 0.5 rad/s (Case 4). (i) $\Delta\omega_g$ is -1 rad/s (Case 5). (j) $\Delta\omega_g$ is 1 rad/s (Case 5). (k) ΔP_0 is 200 W (Case 6). (l) ΔP_0 is -200W (Case 6).

TABLE II
RESULTS OF COMPARISON

Control Method	$\Delta\omega_g = -1$ rad/s(Situation 1)		$\Delta P_0 = -2$ kW(200W)(Situation 2)		$\Delta\omega_g = -1$ rad/s(Situation 3)		$\Delta P_0 = -2$ kW(200W)(Situation 4)	
	Maximum RoCoF	Frequency Overshoot	Maximum RoCoF	Frequency Overshoot	Maximum RoCoF	Frequency Overshoot	Maximum RoCoF	Frequency Overshoot
Proposed	0.550 Hz/s	0.080 rad/s	0.550 Hz/s	0.120 rad/s	0.660 Hz/s	0.040 rad/s	0.660 Hz/s	0.120 rad/s
VSG	0.869 Hz/s	0.246 rad/s	1.225 Hz/s	0.524 rad/s	0.939 Hz/s	0.157 rad/s	1.981 Hz/s	0.593 rad/s
[25]	0.705 Hz/s	0.209 rad/s	0.846 Hz/s	0.417 rad/s	0.803 Hz/s	0.127 rad/s	1.499 Hz/s	0.495 rad/s
[28]	0.796 Hz/s	0.210 rad/s	0.743 Hz/s	0.432 rad/s	0.876 Hz/s	0.129 rad/s	1.151 Hz/s	0.491 rad/s
[30]	0.674 Hz/s	0.198 rad/s	0.844 Hz/s	0.412 rad/s	0.763 Hz/s	0.118 rad/s	1.482 Hz/s	0.484 rad/s
[31]	0.635 Hz/s	0.194 rad/s	0.843 Hz/s	0.407 rad/s	0.742 Hz/s	0.117 rad/s	1.546 Hz/s	0.489 rad/s

corresponding articles, which are not repeated here. Simulation and experiment results are listed in Table II and their waveforms are shown in Figs. 13–18.

As listed in Table II, the proposed control achieves a lower RoCoF and frequency overshoot compared to existing controls. For the step decrease of the grid frequency, compared with the other controls, the maximum RoCoF decreases by $11.1\sim36.7\%$, and the frequency overshoot decreases by $58.8\sim74.5\%$. For the step decrease of the active power reference, compared with the other controls, the maximum RoCoF decreases by $26.0\sim66.7\%$, the frequency overshoot decreases by $70.5\sim79.8\%$, and only the proposed control has no active power overshoot. Compared with existing similar controls, the proposed control can improve the performance of the inverter, which is the same as the comparison by theory.

Except for the aforementioned contents, the total energy injected by the inverter is discussed. In a typical duration time of primary frequency modulation, such as 30 s, the average active power output for the inverter with different controls is compared. In the simulation, in situation 1, the average output power of inverters with the proposed control and the other five chosen controls are 4.010, 4.003, 4.003, 4.004, 4.004, and 4.004 kW, respectively. In situation 2, they are 2.028, 2.006, 2.009, 2.009, 2.008, and 2.008 kW, respectively. In the aforementioned two situations, the maximum difference is 1.01% and the average output powers of the inverter with all control

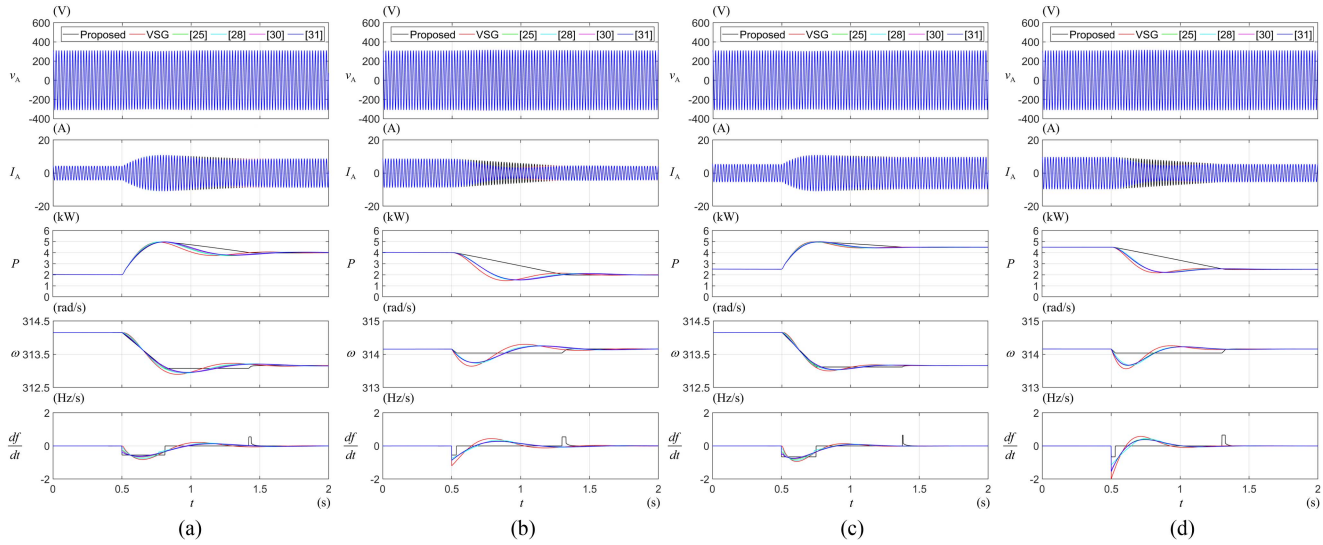

Fig. 13. Simulation waveforms of the inverter with different controls. (a) $\Delta\omega_{\mathrm{g}}$ is -1 rad/s (Situation 1). (b) ΔP_0 is -2 kW (Situation 2). (c) $\Delta\omega_{\mathrm{g}}$ is -1 rad/s (Situation 3). (d) ΔP_0 is -2 kW (Situation 4).

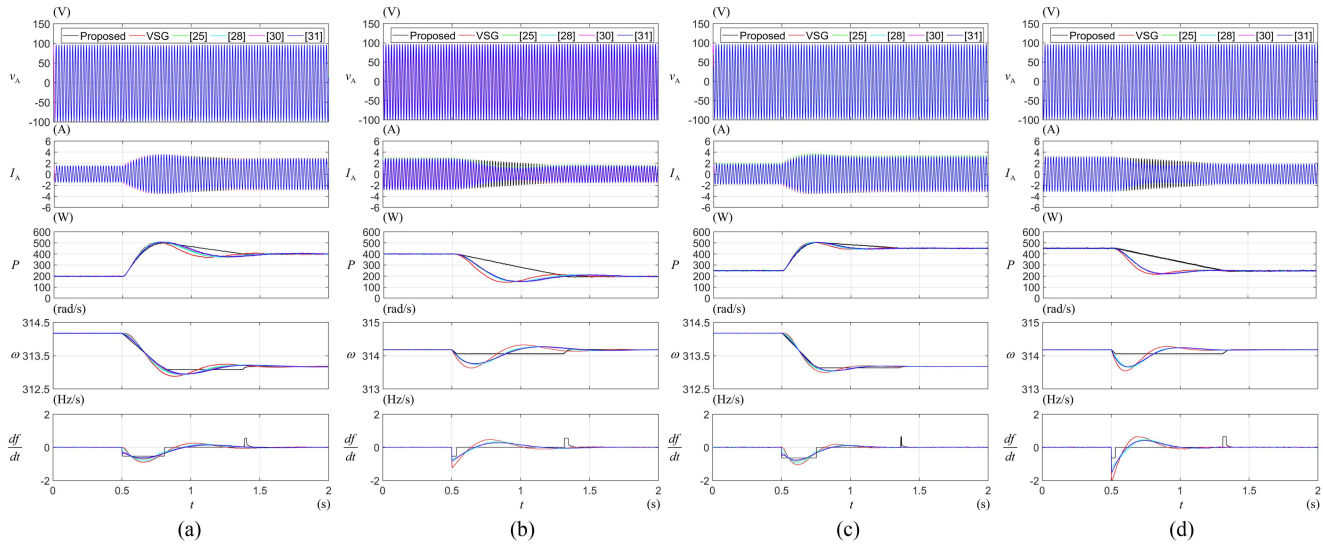

Fig. 14. Combined experiment waveforms of the inverter with different controls. (a) $\Delta\omega_{\mathrm{g}}$ is -1 rad/s (Situation 1). (b) ΔP_0 is -200 W (Situation 2). (c) $\Delta\omega_{\mathrm{g}}$ is -1 rad/s (Situation 3). (d) ΔP_0 is -200 W (Situation 4).

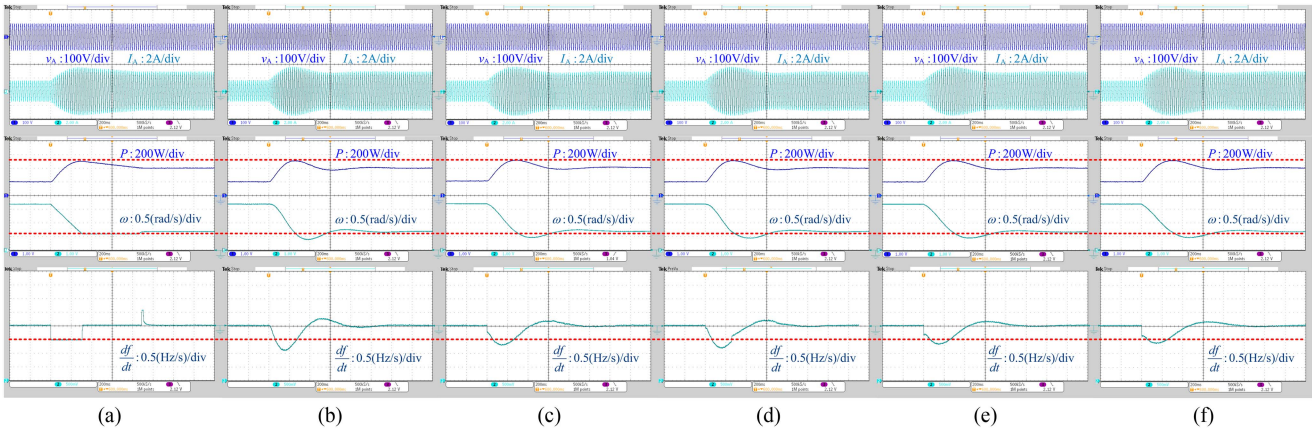

Fig. 15. Separate experiment waveforms of the inverter with different controls in situation 1. (a) Proposed control. (b) Original VSG control. (c) Generalized droop control. (d) Self-adaptive VSG control. (e) Fractional-order VSG control. (f) H_∞ control.

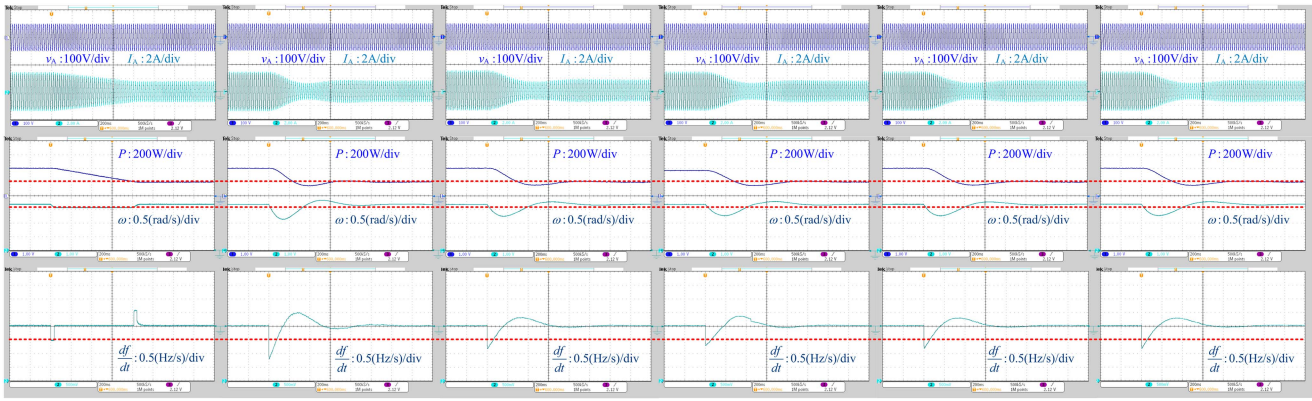

Fig. 16. Separate experiment waveforms of the inverter with different controls in situation 2. (a) Proposed control. (b) Original VSG control. (c) Generalized droop control. (d) Self-adaptive VSG control. (e) Fractional-order VSG control. (f) H_∞ control.

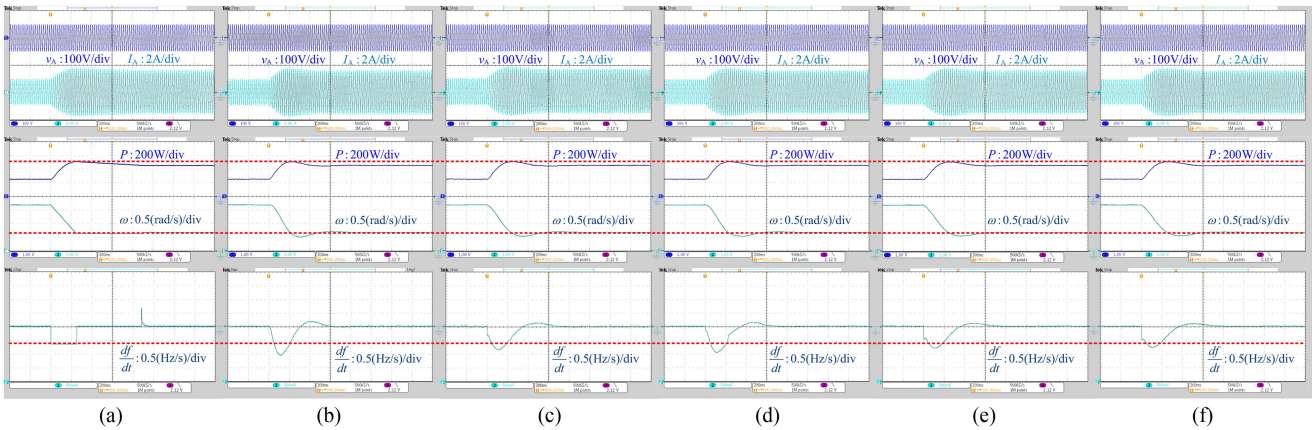

Fig. 17. Separate experiment waveforms of the inverter with different controls in situation 3. (a) Proposed control. (b) Original VSG control. (c) Generalized droop control. (d) Self-adaptive VSG control. (e) Fractional-order VSG control. (f) H_∞ control.

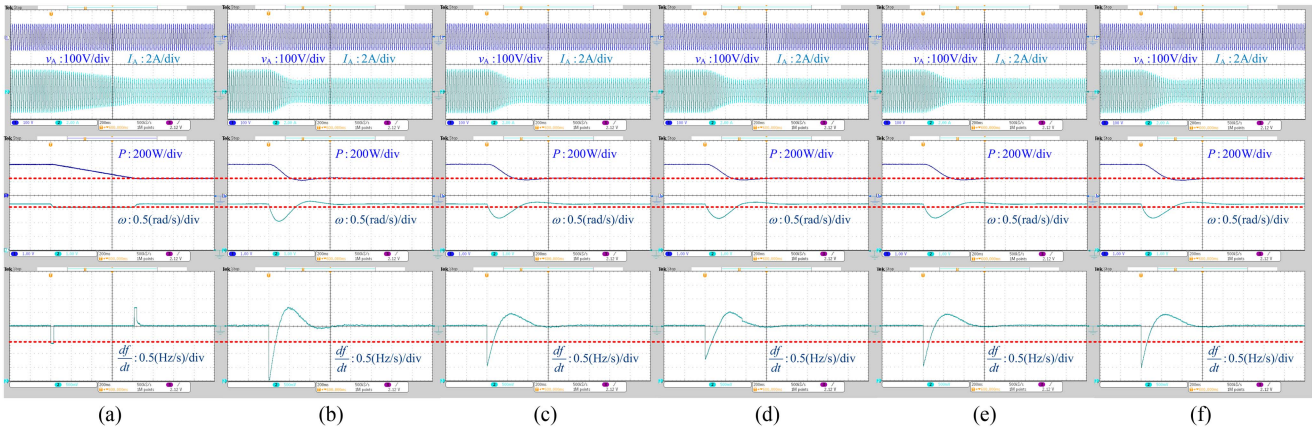

Fig. 18. Separate experiment waveforms of the inverter with different controls in situation 4. (a) Proposed control. (b) Original VSG control. (c) Generalized droop control. (d) Self-adaptive VSG control. (e) Fractional-order VSG control. (f) H_∞ control.

methods are similar. Similar results can also be obtained by the experiment and other situations, which are not expanded here. In this article, the proposed control and other chosen controls mainly influence the transient state of the inverter. However, the average output power is mainly decided by the parameters of the steady state, such as the droop coefficient and the output power reference. As the transient state is much shorter than the steady state, the influences of the aforementioned controls on the average performance of the inverter are almost the same.

VI. Conclusion

In this article, to enhance the frequency stability, the active power control of the grid-connected inverter is designed by the switched control theory. And a switched active power control with reduced RoCoF and frequency overshoot is obtained. The proposed control has the following advantages. First, the proposed control allows for direct adjustment of the maximum RoCoF and frequency overshoot of the inverter, thereby enhancing frequency stability. Next, as analyzed by the Lyapunov theorem of stability, for the active power control loop, the inverter with the proposed control has global asymptotic stability. Then, due to the clear physical meaning of the proposed control, the parameters of the proposed controller can be directly designed using the derived analytical equations, simplifying proposed control's application. Finally, compared with existing controls, the proposed control has the lowest RoCoF and frequency overshoot. In the simulation and experiments, the maximum RoCoF decreases by $11.1\sim66.7\%$ and the frequency overshoot decreases by $58.8\sim79.8\%$. Due to the aforementioned advantage, when better frequency stability is needed, the proposed control is a potential alternative to the traditional VSG control and other improved VSG controls used in grid-connected inverters.

Appendix

In the appendix, it is shown that the chosen control methods can be expressed as the standard state-space model with special control laws in (36).

A. VSG Controls

For the original VSG control [23] and self-adaptive VSG controls [28], although the values of the inertia J and damping D in different VSG controls are different, their active power control loop can be expressed as the unified form

$$\dot{\omega} = \frac{P_0 - P - k_{\mathrm{p}}(\omega - \omega_0) - D(\omega - \omega_{\mathrm{g}})}{J\omega_0}. \tag{A1}$$

With the standard state-space model, the active power loop of VSG controls is transferred into

$$\begin{cases} \dot{\mathbf{x}} = \mathbf{A}\mathbf{x} + \mathbf{B}u \\ u = -\frac{1}{J\omega_0}\Delta P - \frac{D+k_{\mathrm{p}}}{J\omega_0}\Delta\omega \end{cases}. \tag{A2}$$

As shown in (A2), VSG controls are the standard state-space model with two-order state feedback control laws.

B. Generalized Droop Control

For the generalized droop control [25], the active power control loop is

$$\frac{\Delta\omega(s)}{\Delta P(s)} = -G(s) = -\sum_{i=0}^{m-1} a_i s^i \Big/ \sum_{i=0}^{m} b_i s^i. \tag{A3}$$

Making the derivation of $\Delta\omega$ in (A3), the transfer function between $u(s)$ and $\Delta P(s)$ is

$$\frac{u(s)}{\Delta P(s)} = -sG(s) = -\sum_{i=1}^{m} a_{i-1} s^i \Big/ \sum_{i=0}^{m} b_i s^i. \tag{A4}$$

In the time domain, with the standard state-space model, the transfer function in (A4) can be expressed as state-space equation form, which is signed as

$$\begin{cases} \dot{\mathbf{x}} = \mathbf{A}\mathbf{x} + \mathbf{B}u \\ \dot{\mathbf{x}}_{\mathrm{C}} = \mathbf{A}_{\mathrm{C}}\mathbf{x}_{\mathrm{C}} + \mathbf{B}_{\mathrm{C}}\Delta P \\ u = \mathbf{C}_{\mathrm{C}}\mathbf{x}_{\mathrm{C}} + \mathbf{D}_{\mathrm{C}}\Delta P \end{cases} \tag{A5}$$

where $\mathbf{x}_{\mathrm{C}}$, $\mathbf{A}_{\mathrm{C}}$, $\mathbf{B}_{\mathrm{C}}$, $\mathbf{C}_{\mathrm{C}}$, and $\mathbf{D}_{\mathrm{C}}$ are the state vector, state matrix, input matrix, output matrix, and direct transfer matrix of the controller.

The detailed process of transferring the transfer function into the state-space equation can be completed with the general principle of the modern control theory, which is not expanded here. As shown in (A5), the generalized droop control can be expressed as the standard state-space model with high-order state feedback control laws.

C. Fractional-Order VSG Control

For the fractional-order VSG control [30], the active power control loop is

$$\frac{\Delta\omega(s)}{\Delta P(s)} = -\frac{1}{Ms^{\gamma+\lambda} + D_1 s^{\gamma} + D_2} \tag{A6}$$

where γ, λ, M, D_1, and D_2 are parameters of the controller, whose definition can be found in [30].

As the fractional-order s in (A6) is achieved by the expansion of the integer order s [30], the transfer function in (A6) can be transferred into the same form as the transfer function in (A3). Although their parameters are different, the analysis of the generalized droop control is also suitable for the fractional-order VSG control, which can be expressed as the standard state-space model with high-order state feedback control laws.

D. H_∞ Control

For the H_∞ control [31], the active power control loop is

$$\frac{\Delta\omega(z)}{\Delta P(z)} = \frac{x_2 z^2 + x_1 z + x_0}{z^2 + y_1 z + y_0} \tag{A7}$$

where x_2, x_1, x_0, y_1, and y_0 are parameters of the controller, whose definition can be found in [31].

With the bilinear transformation, the transfer function in the z-domain can be transferred into the s-domain, which has the same form as the transfer function in (A3). Then, the analysis of the generalized droop control is also suitable for the H_∞ control, which can be expressed as the standard state-space model with high-order state feedback control laws.

References

[1] X. Zhang et al., "A grid-supporting strategy for cascaded H-bridge PV converter using VSG algorithm with modular active power reserve," *IEEE Trans. Ind. Electron.*, vol. 68, no. 1, pp. 186–197, Jan. 2021.

[2] X. Quan et al., "Photovoltaic synchronous generator: Architecture and control strategy for a grid-forming PV energy system," *IEEE J. Emerg. Sel. Topics Power Electron.*, vol. 8, no. 2, pp. 936–948, Jun. 2020.

[3] J. Liu, F. Tang, J. Zhao, D. Liu, and I. Kamwa, "Coherency identification for wind-integrated power system using virtual synchronous motion equation," *IEEE Trans. Power Syst.*, vol. 35, no. 4, pp. 2619–2630, Jul. 2020.

[4] Z. Zhang, M. Zhou, Z. Wu, S. Liu, Z. Guo, and G. Li, "A frequency security constrained scheduling approach considering wind farm providing frequency support and reserve," *IEEE Trans. Sustain. Energy*, vol. 13, no. 2, pp. 1086–1100, Apr. 2022.
[5] M. Kheshti, S. Lin, X. Zhao, L. Ding, M. Yin, and V. Terzija, "Gaussian distribution-based inertial control of wind turbine generators for fast frequency response in low inertia systems," *IEEE Trans. Sustain. Energy*, vol. 13, no. 3, pp. 1641–1653, Jul. 2022.
[6] D. Yazdani, A. Bakhshai, G. Joos, and M. Mojiri, "A nonlinear adaptive synchronization technique for grid-connected distributed energy sources," *IEEE Trans. Power Electron.*, vol. 23, no. 4, pp. 2181–2186, Jul. 2008.
[7] J. Rocabert, A. Luna, F. Blaabjerg, and P. Rodríguez, "Control of power converters in AC microgrids," *IEEE Trans. Power Electron.*, vol. 27, no. 11, pp. 4734–4749, Nov. 2012.
[8] T. Shintai, Y. Miura, and T. Ise, "Oscillation damping of a distributed generator using a virtual synchronous generator," *IEEE Trans. Power Deliv.*, vol. 29, no. 2, pp. 668–676, Apr. 2014.
[9] S. Negri, E. Tironi, and D. S. Danna, "Integrated control strategy for islanded operation in smart grids: Virtual inertia and ancillary services," *IEEE Trans. Ind. Appl.*, vol. 55, no. 3, pp. 2401–2411, May/Jun. 2019.
[10] C. Li, Y. Yang, N. Mijatovic, and T. Dragičević, "Frequency stability assessment of grid-forming VSG in framework of MPME with feedforward decoupling control strategy," *IEEE Trans. Ind. Electron.*, vol. 69, no. 7, pp. 6903–6913, Jul. 2022.
[11] M. C. Chandorkar, D. M. Divan, and R. Adapa, "Control of parallel connected inverters in standalone AC supply systems," *IEEE Trans. Ind. Appl.*, vol. 29, no. 1, pp. 136–143, Jan./Feb. 1993.
[12] K. D. Brabandere, B. Bolsens, J. V. Keybus, A. Woyte, J. Driesen, and R. Belmans, "A voltage and frequency droop control method for parallel inverters," *IEEE Trans. Power Electron.*, vol. 22, no. 4, pp. 1107–1115, Jul. 2007.
[13] H. Nikkhajoei and R. H. Lasseter, "Distributed generation interface to the CERTS microgrid," *IEEE Trans. Power Del.*, vol. 24, no. 3, pp. 1598–1608, Jul. 2009.
[14] C. Li et al., "New framework of RoCoF-FD for wideband stability evaluation in renewable energy generators with virtual impedance control," *IEEE Trans. Smart Grid*, vol. 13, no. 5, pp. 3570–3581, Sep. 2022.
[15] P. Daly, H. W. Qazi, and D. Flynn, "RoCoF-constrained scheduling incorporating non-synchronous residential demand response," *IEEE Trans. Power Syst.*, vol. 34, no. 5, pp. 3372–3383, Sep. 2019.
[16] M. Chen, D. Zhou, and F. Blaabjerg, "Modelling, implementation, and assessment of virtual synchronous generator in power systems," *J. Modern Power Syst. Clean Energy*, vol. 8, no. 3, pp. 399–411, May 2020.
[17] M. Grebla, J. Yellajosula, and H. K. Høidalen, "Adaptive frequency estimation method for ROCOF islanding detection relay," *IEEE Trans. Power Del.*, vol. 35, no. 4, pp. 1867–1875, Aug. 2020.
[18] S. Chen, Y. Sun, H. Han, G. Shi, Y. Guan, and J. M. Guerrero, "Dynamic frequency performance analysis and improvement for parallel VSG systems considering virtual inertia and damping coefficient," *IEEE J. Emerg. Sel. Topics Power Electron.*, vol. 11, no. 1, pp. 478–489, Feb. 2023.
[19] Z. Zhang, J. Fang, C. Dong, C. Jin, and Y. Tang, "Enhanced grid frequency and dc-link voltage regulation in hybrid ac/dc microgrids through bidirectional virtual inertia support," *IEEE Trans. Ind. Electron.*, vol. 70, no. 7, pp. 6931–6940, Jul. 2023.
[20] H. -P. Beck and R. Hesse, "Virtual synchronous machine," in *Proc. 9th Int. Conf. Elect. Power Qual. Utilisation*, Barcelona, Spain, 2007, pp. 1–6.
[21] Q. Zhong and G. Weiss, "Synchronverters: Inverters that mimic synchronous generators," *IEEE Trans. Ind. Electron.*, vol. 58, no. 4, pp. 1259–1267, Apr. 2011.
[22] Q. Zhong, P. Nguyen, Z. Ma, and W. Sheng, "Self-synchronized synchronverters: Inverters without a dedicated synchronization unit," *IEEE Trans. Power Electron.*, vol. 29, no. 2, pp. 617–630, Feb. 2014.
[23] J. Liu, Y. Miura, and T. Ise, "Comparison of dynamic characteristics between virtual synchronous generator and droop control in inverter-based distributed generators," *IEEE Trans. Power Electron.*, vol. 31, no. 5, pp. 3600–3611, May 2016.
[24] K. Zhuang, H. Xin, P. Hu, and Z. Wang, "Current saturation analysis and anti-windup control design of grid-forming voltage source converter," *IEEE Trans. Energy Convers.*, vol. 37, no. 4, pp. 2790–2802, Dec. 2022.
[25] X. Meng, J. Liu, and Z. Liu, "A generalized droop control for grid-supporting inverter based on comparison between traditional droop control and virtual synchronous generator control," *IEEE Trans. Power Electron.*, vol. 34, no. 6, pp. 5416–5438, Jun. 2019.
[26] J. Alipoor, Y. Miura, and T. Ise, "Power system stabilization using virtual synchronous generator with alternating moment of inertia," *IEEE J. Emerg. Sel. Topics Power Electron.*, vol. 3, no. 2, pp. 451–458, Jun. 2015.
[27] M. Li, W. Huang, N. Tai, L. Yang, D. Duan, and Z. Ma, "A dual-adaptivity inertia control strategy for virtual synchronous generator," *IEEE Trans. Power Syst.*, vol. 35, no. 1, pp. 594–604, Jan. 2020.
[28] F. Wang, L. Zhang, X. Feng, and H. Guo, "An adaptive control strategy for virtual synchronous generator," *IEEE Trans. Ind. Appl.*, vol. 54, no. 5, pp. 5124–5133, Sept./Oct. 2018.
[29] D. Li, Q. Zhu, S. Lin, and X. Y. Bian, "A self-adaptive inertia and damping combination control of VSG to support frequency stability," *IEEE Trans. Energy Convers.*, vol. 32, no. 1, pp. 397–398, Mar. 2017.
[30] Y. Yu, Y. Guan, W. Kang, S. K. Chaudhary, J. C. Vasquez, and J. M. Guerrero, "Fractional order virtual synchronous generator," *IEEE Trans. Power Electron.*, vol. 38, no. 6, pp. 6874–6879, Jun. 2023.
[31] D. B. Rathnayake, S. P. Me, R. Razzaghi, and B. Bahrani, "H_∞-based control design for grid-forming inverters with enhanced damping and virtual inertia," *IEEE J. Emerg. Sel. Topics Power Electron.*, vol. 11, no. 2, pp. 2311–2325, Apr. 2023.
[32] T. Wildi, *Electrical Machines, Drives and Power Systems*, 6th ed. Englewood Cliffs, NJ, USA: Prentice-Hall, 2005.
[33] B. Liu and W. Tang, *Modern Control Theory*, 3rd ed. Beijing, China: China Machine Press, 2006.
[34] G. C. Layek, *An Introduction to Dynamical Systems and Chaos*, Berlin, Germany: Springer, 2015.
[35] J. Chen and T. O'Donnell, "Parameter constraints for virtual synchronous generator considering stability," *IEEE Trans. Power Syst.*, vol. 34, no. 3, pp. 2479–2481, May 2019.
[36] A. J. Sonawane and A. C. Umarikar, "Small-signal stability analysis of PV-based synchronverter including PV operating modes and DC-link voltage controller," *IEEE Trans. Ind. Electron.*, vol. 69, no. 8, pp. 8028–8039, Aug. 2022.
[37] *International Electrotechnical Vocabulary*, IEC Standard 60050, 2001.
[38] S. Skander-Mustapha, M. J. Ghorbal, M. B. Said-Romdhane, M. Miladi, and I. Slama-Belkhodja, "Grid emulator for small scale distributed energy generation laboratory," *Sustain. Cities Soc.*, vol. 43, pp. 325–338, Sep. 2018.
[39] T. Liu, D. Wang, and K. Zhou, "High-performance grid simulator using parallel structure fractional repetitive control," *IEEE Trans. Power Electron.*, vol. 31, no. 3, pp. 2669–2679, Mar. 2016.

Yuan Chen was born in Shandong, China, in 1996. He received the B.S. degree in electrical engineering and automation in 2018 from the School of Electric Power, South China University of Technology, Guangzhou, China, where he is currently working toward the Ph.D. degree in electrical engineering.

His research interests include topology, nonlinear analysis, and control of power electronics.

Bo Zhang (Fellow, IEEE) was born in Shanghai, China, in 1962. He received the B.S. degree in electrical engineering from Zhejiang University, Hangzhou, China, in 1982, the M.S. degree in power electronics from Southwest Jiaotong University, Chengdu, China, in 1988, and the Ph.D. degree in power electronics from the Nanjing University of Aeronautics and Astronautics, Nanjing, China, in 1994.

He is currently a Professor with the School of Electric Power, South China University of Technology, Guangzhou, China. He has authored or coauthored more than 600 papers and held more than 230 patents. He has authored nine monographs. His research interests include nonlinear analysis and control of power electronics, wireless power transfer technology, and ac drives.

Dongyuan Qiu (Senior Member, IEEE) was born in China in 1972. She received the B.Sc. and M.Sc. degrees in automation from the South China University of Technology, Guangzhou, China, in 1994 and 1997, respectively, and the Ph.D. degree in electronic engineering from the City University of Hong Kong, Kowloon, Hong Kong, in 2002.

She is currently a Professor with the School of Electric Power, South China University of Technology. She has authored or co-authored three books and more than 200 papers and holds about 100 patents. Her main research interests include modeling of power electronic converters, wireless power transfer and fault diagnosis.

Dr. Qiu is an Associate Editor for IEEE TRANSACTIONS ON POWER ELECTRONICS.

Yanfeng Chen (Member, IEEE) received the M.S. degree in power electronics technology from Wuhan University, Wuhan, China, in 1995, and the Ph.D. degree in circuits and systems from the South China University of Technology, Guangzhou, China, in 2000.

From 2005 to 2006, she was a Research Associate with the Department of Electronic and Information Engineering, Hong Kong Polytechnic University, Hong Kong. She is currently a Professor with the School of Electric Power, South China University of Technology. She has authored or coauthored three books, and more than 50 papers and 50 patents. Her main research interests include modeling and analysis of nonlinear systems and power electronics.

Fan Xie (Member, IEEE) received the B.S. and M.S. degrees in physics and physical electronics from the School of Physics and Electron Engineering, Guangzhou University, Guangzhou, China, in 2008 and 2011, respectively, and the Ph.D. degree in power electronics from the South China University of Technology, Guangzhou, in 2014.

In 2014, he joined the School of Electric Power, South China University of Technology, where he has been an Associate Professor since 2018. His research interests include nonlinear dynamics of power electronic circuits and control of power supplies and ac drives.

Huadong Sun (Senior Member, IEEE) was born in 1975. He received the B.Eng. and master's degrees from Shandong University, Jinan, China, in 1999 and 2002, respectively, and the Ph.D. degree from China Electric Power Research Institute (CEPRI), Beijing, China, in 2005, all in electrical engineering.

He is currently a Professor of electrical engineering with CEPRI. He is also the Vice President of CEPRI. His research interests include power system analysis and control, stability of power-electronic-based power system, and large-scale renewable power generation and integration.